

PAPER • OPEN ACCESS

A lightweight learning-based decoding algorithm for intraneuronal vagus nerve activity classification in pigs

To cite this article: Leonardo Pollina *et al* 2022 *J. Neural Eng.* **19** 046033

View the [article online](#) for updates and enhancements.

You may also like

- [Bioelectronic medicine for the autonomic nervous system: clinical applications and perspectives](#)

Marina Cracchiolo, Matteo Maria Ottaviani, Alessandro Panarese et al.

- [Artificial referred sensation in upper and lower limb prosthesis users: a systematic review](#)

Michael Gonzalez, Alex Bismuth, Christina Lee et al.

- [Compliant peripheral nerve interfaces](#)

Valentina Paggi, Outman Akouissi, Silvestro Micera et al.

Journal of Neural Engineering



OPEN ACCESS

PAPER

A lightweight learning-based decoding algorithm for intraneuronal vagus nerve activity classification in pigs

RECEIVED
11 April 2022REVISED
18 July 2022ACCEPTED FOR PUBLICATION
27 July 2022PUBLISHED
11 August 2022

Original Content from this work may be used under the terms of the Creative Commons Attribution 4.0 licence.

Any further distribution of this work must maintain attribution to the author(s) and the title of the work, journal citation and DOI.

Leonardo Pollina^{1,2,6}, Fabio Vallone^{1,6,*}, Matteo M Ottaviani^{1,3}, Ivo Strauss¹, Lucia Carlucci³, Fabio A Recchia^{3,4,5}, Silvestro Micera^{1,2,7} and Sara Moccia^{1,7}

¹ The BioRobotics Institute and the Department of Excellence in Robotics and Artificial Intelligence, Scuola Superiore Sant'Anna, Pisa, Italy

² Bertarelli Foundation Chair in Translational Neural Engineering, Center for Neuroprosthetics and Institute of Bioengineering, Ecole Polytechnique Federale de Lausanne, Lausanne, Switzerland

³ Institute of Life Sciences, Scuola Superiore Sant'Anna, Pisa, Italy

⁴ Fondazione Toscana Gabriele Monasterio, Pisa, Italy

⁵ Cardiovascular Research Center, Lewis Katz School of Medicine at Temple University, Philadelphia, PA, United States of America

⁶ Equally contributed first authors.

⁷ Equally contributed senior authors.

* Author to whom any correspondence should be addressed.

E-mail: fabio.vallone@santannapisa.it

Keywords: bioelectronic medicine, vagus nerve, intraneuronal electrodes, real-time decoding algorithm

Supplementary material for this article is available [online](#)



Abstract

Objective. Bioelectronic medicine is an emerging field that aims at developing closed-loop neuromodulation protocols for the autonomic nervous system (ANS) to treat a wide range of disorders. When designing a closed-loop protocol for real time modulation of the ANS, the computational execution time and the memory and power demands of the decoding step are important factors to consider. In the context of cardiovascular and respiratory diseases, these requirements may partially explain why closed-loop clinical neuromodulation protocols that adapt stimulation parameters on patient's clinical characteristics are currently missing. **Approach.** Here, we developed a lightweight learning-based decoder for the classification of cardiovascular and respiratory functional challenges from neural signals acquired through intraneuronal electrodes implanted in the cervical vagus nerve (VN) of five anaesthetized pigs. Our algorithm is based on signal temporal windowing, nine handcrafted features, and random forest (RF) model for classification. Temporal windowing ranging from 50 ms to 1 s, compatible in duration with cardio-respiratory dynamics, was applied to the data in order to mimic a pseudo real-time scenario. **Main results.** We were able to achieve high balanced accuracy (BA) values over the whole range of temporal windowing duration. We identified 500 ms as the optimal temporal windowing duration for both BA values and computational execution time processing, achieving more than 86% for BA and a computational execution time of only \sim 6.8 ms. Our algorithm outperformed in terms of BA and computational execution time a state of the art decoding algorithm tested on the same dataset (Vallone *et al* 2021 *J. Neural Eng.* **18** 0460a2). We found that RF outperformed other machine learning models such as support vector machines, K-nearest neighbors, and multi-layer perceptrons. **Significance.** Our approach could represent an important step towards the implementation of a closed-loop neuromodulation protocol relying on a single intraneuronal interface able to perform real-time decoding tasks and selective modulation of the VN.

1. Introduction

Neuromodulation of the autonomic nervous system (ANS) for the treatment of a broad range of diseases is the goal of an emerging interdisciplinary field named bioelectronic medicine (BM) [1]. The range of potentially treatable diseases includes cardiovascular, respiratory, inflammatory, metabolic and pelvic dysfunctions [2].

The ANS represents a pivotal target for BM applications, as ANS is a key player in the homeostatic control of the body, and influences the evolution of many diseases [2]. Among the branches of the ANS, the vagus nerve (VN) offers a unique opportunity for neuromodulation protocols, as it innervates numerous organs including heart, lungs and stomach, hence modulating vital functions like circulation, respiration and digestion. The electrical stimulation of VN (VNS) has shown promising results, both pre-clinically and clinically, in terms of controlling physiological parameters such as heart rate and blood pressure, and inflammatory levels [2, 3].

Ideal VN neuromodulations for the treatment of diseases in BM would rely on miniaturized electronic devices capable of performing a highly efficient closed-loop peripheral neuromodulation: the stimulation parameters should be tuned in real time based on patients-specific markers deriving from neural signals online recording. One crucial aspect that needs to be evaluated when building a closed-loop protocol is the design of the decoding step, which should achieve high performance at low computational execution time [2–5]. Power consumption and memory demand are indeed crucial aspects to take into account [6]. Challenges in the implementation of closed-loop protocols that match these requirements may partially explain why most of the current therapies are based on open-loop control strategies with levels of stimulation parameters set at the beginning of the treatment.

Few closed-loop VNS protocols have been successfully adopted for seizure suppression by using cardiac-based seizure detection algorithms [7, 8]. However, closed-loop clinical protocols for diseases like cardiovascular, respiratory, inflammatory, metabolic and pelvic dysfunctions are currently missing [2, 3]. Preliminary closed-loop approaches to control the heart rate were proposed by implementing continuous VNS without any cardiac beat synchronization (asynchronous VNS) [9, 10]. In [9], the authors developed a closed-loop approach for the regulation of average ventricular rate during atrial fibrillation in dogs. Asynchronous VNS was delivered to the left VN and stimulation frequency was adjusted based on a cumulative sum control chart technique. A heart rate control strategy for pigs was developed in [10]. Stimulation frequency was adjusted by means of a proportional-integral controller and different

stimulation sites i.e. left and right VN separately or in conjunction were tested [10].

The design of advanced closed-loop VNS protocols for cardiovascular diseases is still limited to a proof-of-concept study on blood pressure control in one anaesthetized rat [4] and a preclinical study on the regulation of the instantaneous heart rate in sheep by adopting a closed-loop protocol based on state transition models [11]. Both studies used cuff electrodes for VNS, while sensors were placed elsewhere to monitor blood pressure and heart rate. Studies on peripheral somatic nerves have shown that cuff electrodes display a low fiber stimulation selectivity [12]. This applies also to autonomic nerves, as indicated by studies on long-term vagal stimulation in humans for the treatment of heart failure [13] and in VN of anesthetized dogs [14]. To date, no studies employing cuff electrodes have shown the possibility to decode cardio-respiratory challenges from VN recordings. However, informative signals from cuff electrodes implanted in pig VN were obtained [15–17]. Specific neurograms related to the respiratory cycle [15], respiratory afferents' spiking activities [16] and blood pressure fluctuation [17] were recorded from pig VN using bipolar/tripolar ring cuff electrodes.

A valuable alternative to cuff electrodes is represented by intraneuronal interfaces which show better stimulation selectivity and signal-to-noise ratio in somatic nerves [12, 18–21]. Similar findings have been reported in experiments involving VN recordings and stimulation paradigms [22–25]. In [23], highly-selective single-fiber intraneuronal recordings were obtained from the human VN using an ultrasound-guided microneurography approach. A recent study [24] has shown the possibility to decode the behavior of freely moving rodents by using an intraneuronal carbon nanotube sensor inserted in the VN. In another study on neural biomarkers inference from intraneuronal VN recording and stimulation of respiratory and blood pressure related fibers in anaesthetized pigs [25], the authors recovered blood pressure and respiratory profiles from VN. A reliable modulation of blood pressure and heart rate was also achieved through suitable stimulation sites of the intraneuronal interface [25]. However, in [25] the authors did not implement a closed-loop stimulation protocol and they did not decode multiple physiological changes of respiratory and/or blood pressure parameters. Our group has recently provided good evidence of the reliability of decoding cardio-respiratory functional challenges from VN activity by using intraneuronal electrodes [22]. However, our decoding algorithm [22] cannot be implemented in real time due to its high computational execution time.

In the present study, we overcome the limitation of our previous decoding algorithm [22]

by proposing a lightweight learning-based decoding algorithm that relies on few handcrafted features and classification via random forest (RF). RF models proved to be efficient in neural decoding tasks, such as detection of epileptic seizures with electroencephalographic signals [26], decoding motor intention using electromyographic data [27] or invasive recordings in peripheral somatic nerves [28], by detecting naturally evoked compound action potential in the sciatic nerve [29], and investigating personal agreement on various statements through functional magnetic resonance imaging (fMRI) [30]. The interest in RF for closed-loop neuromodulation was also due to its suitability for an on-chip integration and on-edge deployment [31, 32].

We tested our new algorithm on a previously collected dataset [22] where different intraneuronal recordings from VN of anaesthetized pigs were acquired during alterations of cardio-respiratory parameters characterizing distinct physiological conditions. We mimicked a pseudo real-time scenario in which signal time windowing was used to resemble incoming data to be classified. The performance of our algorithm was investigated on various sliding window sizes relevant for cardio-respiratory time scale dynamics. Our algorithm significantly outperforms a state of the art decoding algorithm [22] on relevant time scales for cardio-respiratory dynamics by showing a greater decoding accuracy achieved in shorter time.

2. Methods

2.1. Data description

To develop and test our decoding algorithm, we used the dataset collected by our group in [22].

Neural peripheral activity was recorded by using intraneuronal electrodes implanted in the pig cervical VN (figure 1(A)) during a baseline condition and functional cardio-respiratory challenges that modifies physiological parameters, such as mean aortic blood pressure (MAP), tidal volume (TV) and respiratory rate (RR) (figure 1(B)). Functional challenges were induced to reach a target value referred to an increase over a baseline condition. Baseline condition was defined as a period in which MAP and heart rate were stable for at least 30 min after electrode insertion. Specifically, a 150% increase of MAP baseline values obtained with an intravenous infusion of Ang II (vasopressor) lasting for 7–10 min (animal dependent) corresponded to a blood pressure challenge (BPC), whereas 125%–200% of TV baseline values and RR 15–20 br min⁻¹ (baseline 10 br min⁻¹) lasting for 2 min characterized the tidal volume challenge (TVC) and respiration rate challenge (RRC), respectively (figure 1(B) and supplementary figure S1).

Physiological parameters were monitored and recorded by means of electrocardiogram (ECG),

respiratory pressure, arterial systolic, diastolic and mean blood pressure. ECG, aortic blood pressure and respiratory pressure signals were sampled at 24 414 Hz and low-pass filtered with down-sampling (Butterworth fourth-order) at 50 Hz, 25 Hz and 10 Hz, respectively (RZ5D BioAmp Processor, Pz5, Tucker-Davis Technologies Inc. TDT, USA).

Intraneuronal electrodes such as TIME [18] and SELINE [19] were used to record neural activity (figure 1(C)), three pigs (p2, p5, and p6) were implanted with TIME electrodes (p2-t2, p5-t3 and p5-t4, p6-t5 and p6-t6) and other two pigs (p3 and p4) with SELINE interfaces (p3-s1, p4-s3 and p4-s4). The number of active recording channels (N_{ch}) per electrode varied across animal (7 sites (p4-s3), 10 sites (p2-t2), 13 sites (p3-s1,p3-s2,p4-s4) and 16 sites (p5-t3, p5-t4, p6-t5, p6-t6)). Neural signals were recorded with a sampling frequency (f_s) of 24 414 Hz, high pass filtered at 5 Hz and digitally amplified (RZ5D BioAmp Processor, Pz5, Tucker-Davis Technologies Inc. TDT, USA).

In this study, we considered only five animals out of the six considered in [22]. The first animal (p1) which was implanted with a TIME electrode (t1) was discarded due to missing functional respiratory challenges.

2.2. Preprocessing, time windowing and feature extraction

A 4th-order Butterworth filter was used to band-pass filter the recorded signals with cutoff frequencies 1000 Hz and 6000 Hz. These cutoff frequencies were known to contain informative cumulative spiking activity of fiber's population both in autonomic [3, 22, 23] and somatic nerves [20] and discard different artifact sources like electrode's movement, ECG signal [3, 20] and electrical noise [33]. Filtered signals were then sub-sampled by a factor 2. To make our approach more suitable for real-time signal processing and online applications, signal windowing was performed by using a window size (w_s) with overlap (w_o).

For each window, we computed nine handcrafted features: the first four statistical moments (i.e. mean, variance, kurtosis and skewness), wavelength (WL), mean absolute value (MAV), power (POW), maximum value (MAX) and amplitude (AMP). Some of these features were successfully employed in other works [27, 28, 34, 35]. For example, in [35] a subset of the above features were successfully used to decode sensory events from neural activity recorded in the sciatic nerve of rats. The nine features were extracted for all active sites independently and then concatenated to obtain a feature vector of length $N_{active\ sites} \times 9$. The low number of features per time window allowed us to keep the computational execution time low (see figure 2 top left and middle panels).

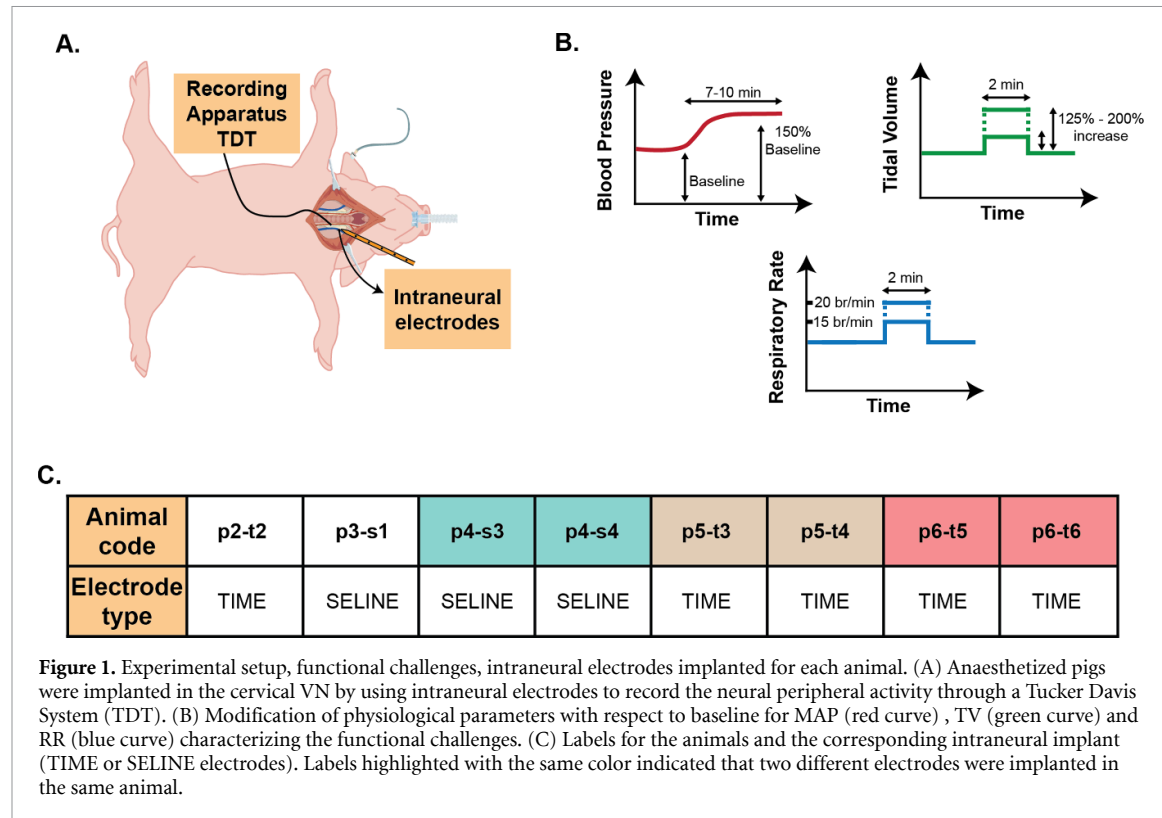


Figure 1. Experimental setup, functional challenges, intraneuronal electrodes implanted for each animal. (A) Anaesthetized pigs were implanted in the cervical VN by using intraneuronal electrodes to record the neural peripheral activity through a Tucker Davis System (TDT). (B) Modification of physiological parameters with respect to baseline for MAP (red curve), TV (green curve) and RR (blue curve) characterizing the functional challenges. (C) Labels for the animals and the corresponding intraneuronal implant (TIME or SELINE electrodes). Labels highlighted with the same color indicated that two different electrodes were implanted in the same animal.

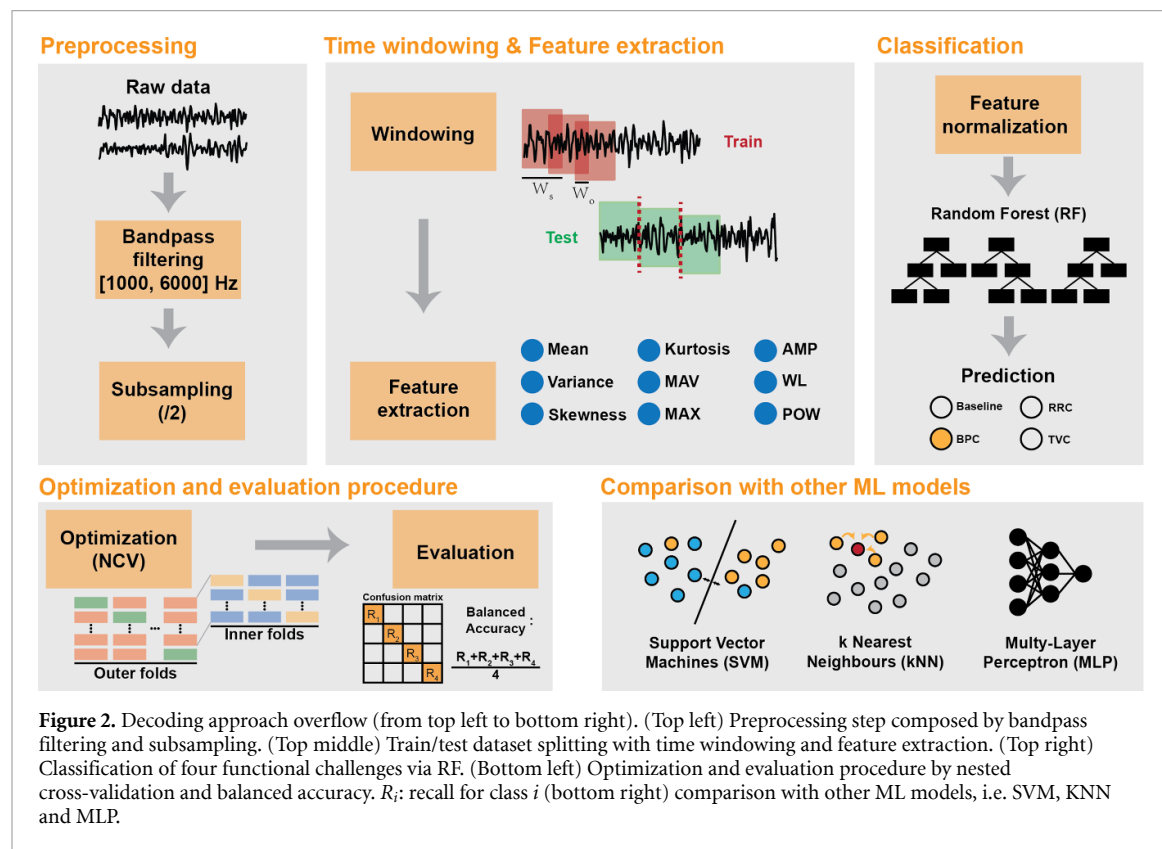


Figure 2. Decoding approach overview (from top left to bottom right). (Top left) Preprocessing step composed by bandpass filtering and subsampling. (Top middle) Train/test dataset splitting with time windowing and feature extraction. (Top right) Classification of four functional challenges via RF. (Bottom left) Optimization and evaluation procedure by nested cross-validation and balanced accuracy. R_i : recall for class i (bottom right) comparison with other ML models, i.e. SVM, KNN and MLP.

2.3. Classification

We selected RF for predicting the challenge associated to each window based on its success throughout several applications and on its efficiency from a computational execution time point of

view [26–30]. Number of trees and tree maximal depth were tuned during training, as explained in section 2.4.

Bootstrap procedure was used when training the classification trees and the weights of the four classes

(baseline, BPC, RRC, TVC) were adjusted to be inversely proportional to each class frequency in order to take into account class imbalance in the dataset due to different time length of the functional challenges (see section 2.1).

Feature extraction and classification with RF was performed at different values of w_s in order to monitor how the performance was affected by the time-window length (see figure 2 top right panel).

2.4. Optimization, evaluation procedure and features importance

A total of five pigs were considered for this study. Each animal was considered independently. A train-test split of 90%–10% was applied to each of the recorded signals, prior performing windowing in order to avoid classification bias. Regarding the windowing procedure, to find the best w_s , several sizes were tested from $w_s = 50$ ms to $w_s = 1$ s with steps of 50 ms. We considered this testing interval to fit our algorithm in a pseudo real-time application scenario in which cardio-respiratory alterations affects blood pressure and respiratory profiles [25]. The minimum value of w_s equal to 50 ms was consistent with systolic times of blood pressure profiles in anaesthetized pigs [25]. Similar to [22], we considered a maximum value for w_s equal to 1 s consistent with inflation/deflation phases of respiratory profiles in anaesthetized pigs [25]. A w_o corresponding to the 20% of the current w_s was used for the training set in order to increase the amount of windows available. No overlap ($w_o = 0$ ms) was used for the testing set.

During training, for each time-window the RF model was fed with a feature vector with dimension $N_{ch} \times 9$, where 9 is the number of features we extracted, as explained in section 2.2. Features were normalized independently across time windows by subtracting the mean and dividing by the standard deviation. Test features were normalized according to the mean and standard deviation estimated on the training set.

To obtain a robust estimation of the RF performance, we performed a nested cross-validation (NCV) with ten outer test folds and five inner validation folds used for hyper-parameters tuning. During training, a grid-search was performed in which the number of trees varied in [50, 100, 200, 400], while their maximal depth in [5, 10, 20].

The best combination of hyper-parameters was selected based on the highest balanced accuracy (*Balanced Accuracy*) on the validation set:

$$\text{Balanced Accuracy} = \frac{1}{J} \sum_{j=1}^{j=J} \text{Rec}_{\text{class}_j} \quad (1)$$

$$\text{Rec}_{\text{class}_j} = \frac{\text{TP}_j}{\text{TP}_j + \text{FN}_j} \text{ for } j \in 1, \dots, 4 \quad (2)$$

being $\text{Rec}_{\text{class}_j}$ the *Recall* for the j th class, TP_j the true positive of the j th class, FN_j the false negative of the j th

class, FP_j the false positive of the j th class, and J the total number of classes. The *Balanced Accuracy* (*BA*) was selected to account for class imbalance in the dataset. Confusion matrices were shown, too (see figure 2 bottom left panel). To study which features contributed most to *BA* we assessed the decrease in tree's impurity quantified by the Gini importance index. We analyzed the indirect contribution to the final *BA* measure of each active sites by summing the decrease in impurity across all features computed for each active site. We ranked active sites by their relative importance in decreasing tree's impurity. To assess the necessary number of active sites to substantially decrease tree's impurity, we cumulatively summed, following active sites' ranking, the contribution to impurity decrease of active sites' pool.

Finally, to gather an idea of the efficiency of our approach from a computational execution time point of view, the time needed to perform both the feature extraction step and the prediction step was measured by streaming the time windows composing the test set one by one for all the ten folds of the NCV for on a sample animal (p2-t2).

2.5. Comparison with other machine learning (ML) models

Our RF classifier was compared with standard and modern machine learning algorithms such as support vector machines (SVMs), k-nearest neighbors (kNNs), and shallow or deep neural networks that have unlocked the possibility to decode neural activity with high accuracy on a wide range of problems [34, 36, 37] (see figure 2 bottom right panel).

For all three models we followed the same routine as we did with the RF classifier. Within the NCV, we optimized each model by tuning the following hyper-parameters: for KNN, the number of neighbors varied in [3, 5, 7, 9, 11, 13]; for SVM, the kernel function was selected between the *radial basis function* (rbf) function or the *sigmoid* function and the L2 regularization value varied in $[1 \times 10^{-2}, 1 \times 10^{-1}, 1]$, with 1 indicating no regularization; for multi layer perceptron (MLP), the three architectures [128, 128, 128], [128, 512, 512, 128], and [128, 256, 512, 512] were tested, where the numbers indicate the number of hidden neurons from the first to the fourth layer. For MLP, training was performed with a learning rate of 1×10^{-3} for 30 epochs and a batch size of 128. For all tested ML models, we repeated the procedure aiming at investigating the effect of w_s on the performance.

Finally, our RF model was also compared to the previous state of the art approach followed in [22].

Analysis were performed on a MacBook Pro (13-inch, 2020, Apple Inc.) with a 2.3 GHz Quad-Core Intel Core i7 processor and a memory of 32 GB. The source code was written in Python 3.8.3, and libraries Scikit-learn 0.23.1, Tensorflow 0.23.1, and SciPy 1.7.1 were used.

2.6. Statistical analysis

The balanced accuracies obtained from electrodes implanted inside the same animal were compared via a permutation test. For each fold the labels indicating the electrode used for the recording were shuffled in order to perform a paired test. Thus, 1024 permutations corresponding to all possible combinations (i.e. $2^{10} = 1024$) were performed. The null distribution was found by computing the following metric:

$$\text{Permutation test metric} = \frac{|\mu_{\text{El.1}} - \mu_{\text{El.2}}|}{\sigma_{\text{El.1}} + \sigma_{\text{El.2}}} \quad (3)$$

where $\mu_{\text{El.1/2}}$ and $\sigma_{\text{El.1/2}}$ represent the average performance and the standard deviation estimated across the ten folds of the NCV for the two electrodes (El.1 and El.2), respectively. The permutation test was performed for all models implemented and for all time windows investigated.

The comparisons among the performances obtained by the different classifiers were performed by using a Kruskal–Wallis test followed by Dunn's post-hoc tests for multiple comparisons.

When comparing the performances of the RF classifier to the ones obtained by our previous approach [22], a paired *t*-test was used. Normality of data distributions were tested via the Shapiro–Wilk test.

3. Results

3.1. RF achieves high accuracy in short time

We first investigated the reliability of our RF learning based approach as a function of the data windowing size w_s (see section 2.2). A time step of 50 ms spans the w_s interval from 50 ms to 1 s. This time interval can be potentially suitable for real-time application since the minimum (50 ms) and maximum (1 s) of the data windowing size w_s were consistent with the systolic time of blood pressure profiles and inflation/deflation phases of respiratory profiles ([25], see section 2.2).

We achieved above chance BA (the average over true positive rate for all classes, see section 2.4) values (i.e. > 25%) for each animal over the whole interval of data windowing size w_s . In figure 3, the BA for each animal and for all different values of w_s is shown.

To check possible effects on BA measure due to electrode positioning and data windowing size, we statistically tested the values of BA for two different electrodes implanted in the same animal for the whole range of w_s values (i.e. p4-s3 vs. p4-s4, p5-t3 vs. p5-t4, and p6-t5 vs. p6-t6, paired permutation test, $n = 1024$ for each animal, see section 2.6). Consistent to [22] we found that the signal recorded in p4-s3 gave significantly better results than p4-s4 throughout all time windows ($p < 0.05$, permutation test, $n = 1024$, see supplementary figure S2 panel A, p4-s3 vs. p4-s4). The case of p5-t4 gave higher BA values than p5-t3 for time windows with $w_s > 100$ ms ($p < 0.05$,

permutation test, $n = 1024$ see supplementary figure S2 panel A, p5-t3 vs. p5-t4). On the contrary, the differences between p6-t5 vs. p6-t6 are statistically significant only for $w_s < 100$ ms ($p < 0.05$, permutation test, $n = 1024$ see supplementary figure S2 panel A, p6-t5 vs. p6-t6). Overall, similar to [22] we found an effect of electrode positioning on decoding performances.

In the following, we reported additional performance metrics for all animals i.e. confusion matrices, median, 1st and 3rd quartiles of the RF classifier across the ten folds and computational efficiency on a sample animal p2-t2 (see section 2.4). In particular, we reported the case of 500 ms for w_s as we consider particularly interesting this value for two reasons. Firstly, by taking into account the importance of keeping w_s as low as possible while maintaining a high decoding accuracy, the value of 500 ms appears to be a good compromise as shown in figure 3 where overall the different median BA curves reach a plateau. Secondly, a temporal scale of 500 ms could be also suitable for real-time applications to detect changes relative to pulse period of blood pressure profiles in anaesthetized pigs [25]. Similar results were found with the different values of w_s (data not shown).

Figure 4 shows the normalized confusion matrices for all animals computed by averaging the performances across the ten folds obtained by the RF classifier when using a w_s of 500 ms. The true class was always predicted in a higher percentage than the false classes. The median value across the ten folds of the NCV for each animal together with the 1st and 3rd quartiles are reported in table 1. Overall, a median BA higher than 86% was reached for all animals.

The time needed to both extract the features and to predict the class for a single time window was measured to evaluate the computational execution time of our classifier. We found that the median values across folds for the 50% and 99% percentiles were indicatively ~ 4.2 ms and ~ 6.8 ms, respectively. To gather some insights in which features contribute most to BA, we leveraged the structure and the intrinsic mechanism of RF to identify the most important features based on the decrease in tree's impurity quantified by the Gini importance index. We consistently found across animals that the most important features were relative to the amplitude of the signal i.e. MAV, variance (VAR), and POW (see figure 5(A) and supplementary figure S7). These results agree with recent findings on the different magnitude of cardiac and respiratory modulations inferred in human VN activity by means of high-selective microneurographic recordings [38]. Moreover, we found that not all active sites contribute equally to the BA measure (see supplementary figure S7). We thus quantified the number of necessary active sites to substantially decrease tree's impurity (see section 2.4). We found that around the 50% of the active sites would already lead to a decrease in impurity of the 80%

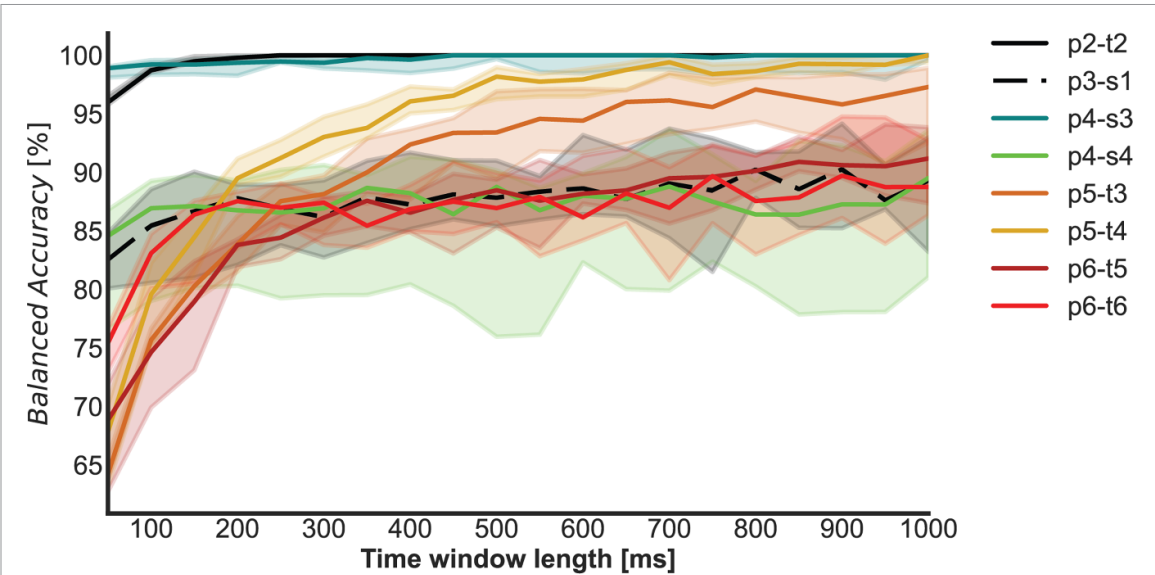


Figure 3. *Balanced Accuracy* obtained by the random forest classifier for each animal and for each time window tested. The duration of the time windows extracted from the signals was incremented by 50 ms starting from an initial duration of 50 ms and reaching a final duration of 1 s. A constant overlap of 20% between consecutive time windows was used. Bold lines indicate median performance, while the faded colored area spans the range from the 1st to the 3rd quartiles across the ten test folds.

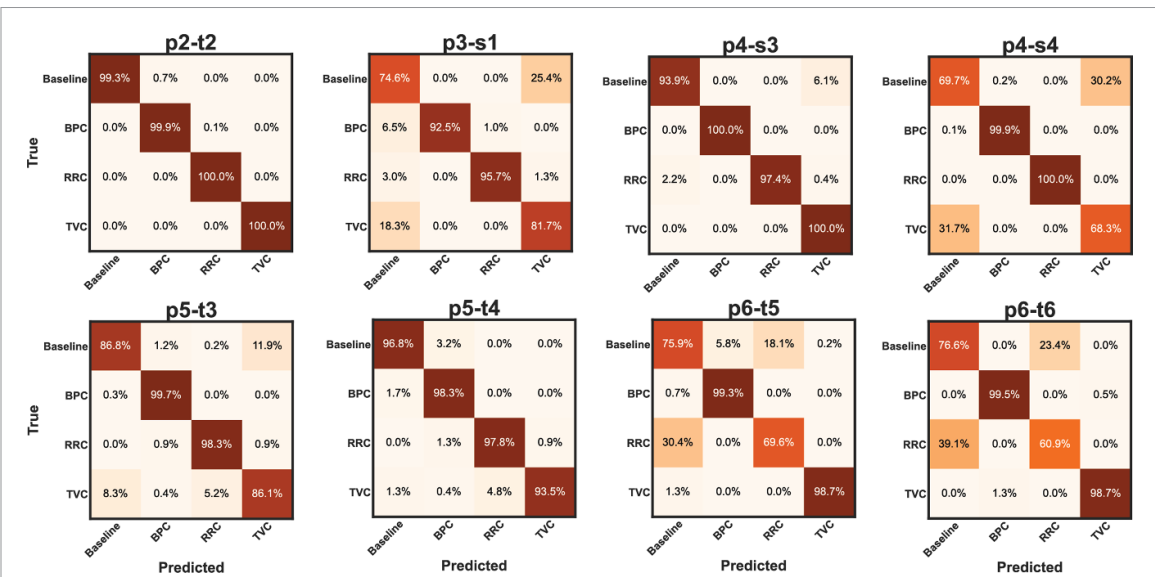


Figure 4. Confusion matrices for all four classes (baseline, BPC, RRC, TVC) and for each animal indicating the performance of the RF model when using time windows of 500 ms (with an overlap of 100 ms). Each confusion matrix is the average across the ten test folds of the nested cross-validation. Values are reported in percentages and are normalized per row (true class).

(see figure 5(B) and supplementary figure S7). This highlights the importance of a multichannel intraneuronal electrode approach, since the presence of multiple active sites increases the likelihood of optimal contact with different types of nerve fibers.

3.2. RF outperforms other ML models and state of the art decoding approach

We compared our RF classifier with other standard ML models such as SVM, MLP and KNN for each animal and over the whole interval of data windowing size w_s (see section 2.5). For all ML tested models, similar to RF classifier, we were able to reach above chance level BA values (i.e. $> 25\%$)

regardless of animal and data windowing size w_s (see supplementary figures S3–S5 panels A for SVM, MLP and KNN, respectively), thus indicating a robustness of our decoding scheme over different classifiers.

When comparing the BA values obtained between different electrodes implanted in the same animal, we found that the difference between p4-s3 and p4-s4 already observed in the RF model was significant for all ML investigated models (paired permutation test, $p < 0.05$, $n = 1024$, see supplementary figure S2 left panels). Moreover, p5-t3 resulted to give performances higher than p5-t4 for $w_s \gtrsim 700$ ms when classifying with the MLP model and for $w_s \lesssim 600$ ms when classifying with KNN. For animal p6 (p6-t5 vs. p6-t6),

Table 1. Median, 1st and 3rd quartiles of the RF classifier across the ten folds for all animals when using $w_s = 500$ ms.

	p2-t2	p3-s1	p4-s3	p4-s4
Median (%)	100.0	87.84	100.0	88.76
25th percentile (%)	100.0	85.4	99.68	75.96
75th percentile (%)	100.0	91.0	100.0	90.15
	p5-t3	p5-t4	p6-t5	p6-t6
Median (%)	93.41	98.18	88.47	86.95
25th percentile (%)	89.47	96.26	85.29	85.74
75th percentile (%)	96.93	98.98	89.37	89.95

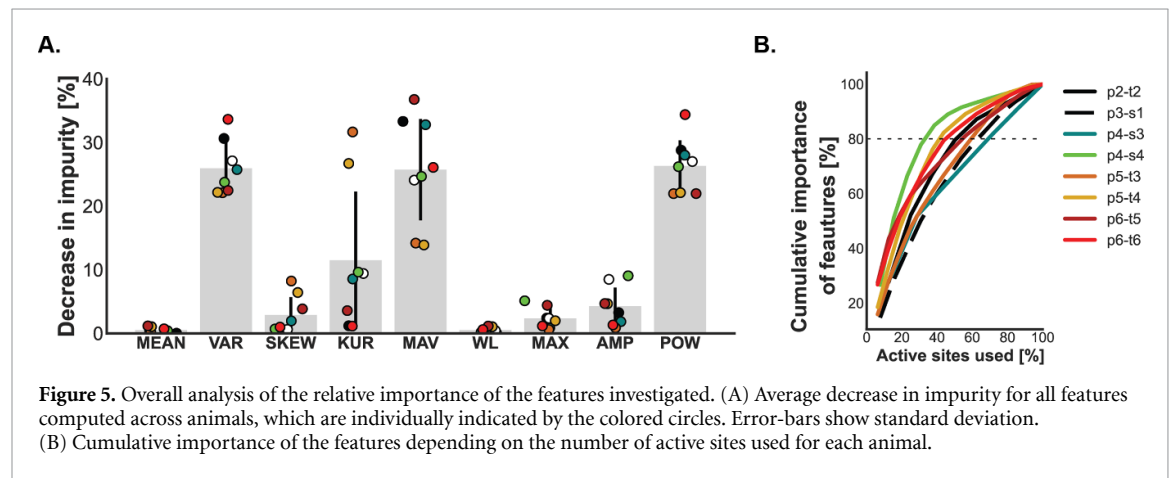


Figure 5. Overall analysis of the relative importance of the features investigated. (A) Average decrease in impurity for all features computed across animals, which are individually indicated by the colored circles. Error-bars show standard deviation. (B) Cumulative importance of the features depending on the number of active sites used for each animal.

p6-t5 yielded better performances than p6-t6 in the case of the MLP classifier for $w_s \gtrsim 600$ ms (paired permutation test, $p < 0.05$, $n = 1024$, supplementary figure S2). To summarize, these results confirm the previous findings on a possible role of electrode positioning on decoding accuracy [22].

For the same two reasons of the previous section and to have a quantitative comparison between RF and the selected ML models, we reported additional performance values in the case of w_s equal to 500 ms i.e. confusion matrices, median, 1st and 3rd quartiles of ML models across the ten folds for all animals. Similar results were found with the different values of w_s (data not shown). Consistently with the results obtained via RF classification, for all ML models the BA measure reached a plateau at w_s equal to 500 ms (see supplementary figures S3–S5 panels A for SVM, MLP and KNN, respectively). Confusion matrices for all animals when setting w_s to 500 ms are shown in supplementary figures S3–S5 panels B for the SVM, MLP and KNN models, respectively. The median value together with the 1st and 3rd quartiles are reported in supplementary tables S1–S3 for the SVM, MLP and KNN models, respectively.

For each animal, figure 6 shows the box-plots representing the distribution of the BA values for all ML models. The distributions of BA values were estimated in each ML model by considering the BA values evaluated in each fold (ten folds).

To compare the RF classifier with the other selected ML models, we pooled together the BA values

of the different folds for the different animals (for each classifier a total number of 80 BA values was obtained). The RF classifier resulted to yields the highest BA measure among all selected ML models ($p < 0.01$, Kruskal–Wallis test followed by Dunn's post-hoc test, $N = 80$). No significant difference was found between the BA values of the SVM and the MLP classifiers. The KNN classifiers turned out to be the model with lowest BA ($p < 0.001$, Kruskal–Wallis test followed by Dunn's post-hoc test, $N = 80$ see supplementary figure S6). We tested the BA values robustness of the considered ML models on the reduction of the training set size. We randomly sampled a certain amount of time windows (i.e. 90%, 80% and 70%) of the total training time windows. The length of the test set was kept constant. What we observed is that the RF still was the best model, showing a greater robustness disregarding the decrease in training samples ($p < 0.05$, Kruskal–Wallis test followed by Dunn's post-hoc test, $N = 80$ see supplementary figure S8).

Finally, we compared the BA values obtained by our previous decoding scheme [22] with the current approach based on RF classification. The BA values obtained by the classification implemented in [22] were such that the 25% quartile, median and 75% quartile were 52.51%, 61.09% and 69.47%, respectively (across the eight recordings). We found that our RF classifier performed significantly better than the previously used strategy (paired t-test, $p < 0.001$, $N = 8$).

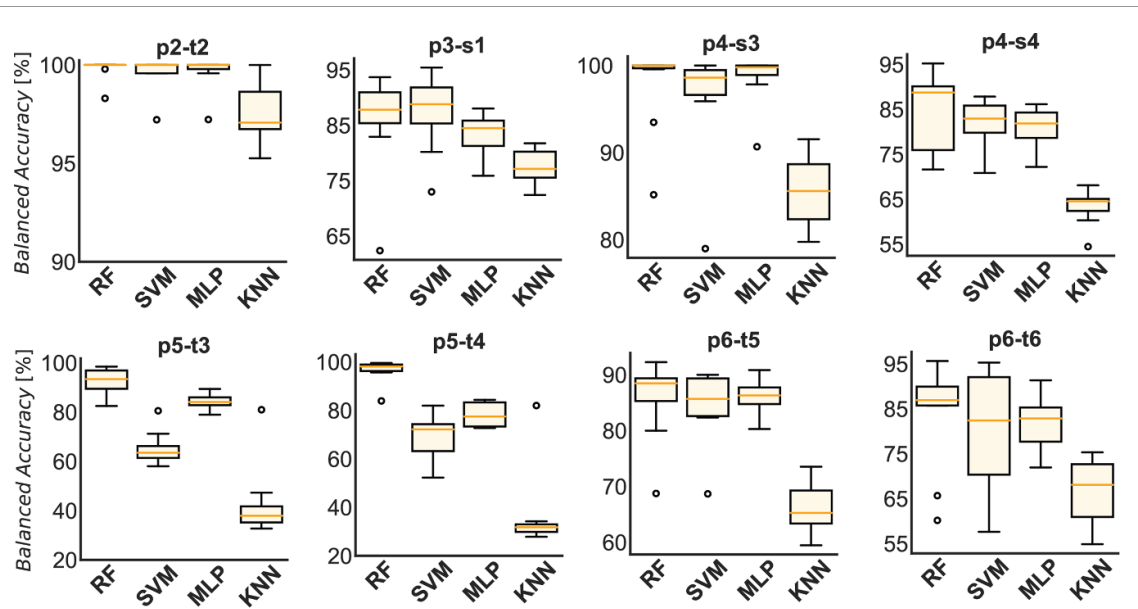


Figure 6. Box-plots representing the distribution of the performances obtained across the ten folds of the nested cross-validation for all classifiers and for each animal separately.

4. Discussion

Real time decoding of peripheral neural signals to monitor changes in physiological parameters is an essential step for closed-loop neuromodulation protocols in BM [1, 2, 4]. Indeed, the stimulation of peripheral fibers must be triggered with a high temporal precision in response to functional alterations. In the present study, we reconsidered a recently published approach for the decoding of intraneurally recorded VN signals during cardiovascular and respiratory alterations in anaesthetized pigs [22]. Our previous decoding algorithm [22] showed to reliably classify cardio-respiratory alterations, yet it was not suitable for real-time applications due to its high computational execution time, hence the need for an alternative approach.

In the current study, we utilized the already published dataset of intraneurally-recorded VN signals associated to cardio-respiratory alterations [22] to develop an efficient pipeline based on a few hand-crafted features and classification via RF suitable for decoding of physiological states with a low computational execution time. We successfully employed the few hand-crafted features previously considered in other research topics [27, 28, 34, 35], such as for example decoding of sensory information from rat sciatic nerves signals [35] and human motor intention by electromyographic (EMG) data [27]. We choose RF as the classifier due to its success in the field of neural decoding tasks applied to fMRI, electroencephalography (EEG), EMG and peripheral nerve activity [26–28, 30, 39]. In particular, in [28] the authors considered features similar to those utilized in our study and RF for the classification step. They were able to decode motor intention with a high level

of accuracy in a human with amputation by using intrafascicular recordings from residual ulnar and median nerves. Moreover, in our previous study [22], we reliable decoded cardio-respiratory alterations of the present dataset by using decision trees combined with random undersampling boosting (RUSBoost), thus promoting decision trees as suitable types of classifiers for the considered decoding task.

We first investigated the performance of our algorithm, deciphered by BA measure, as a function of the time window size used to extract the recorded signals. We considered temporal values potentially suitable for real-time applications on cardio-respiratory dynamics since their range spans relevant time scales of blood pressure and respiratory profiles. Indeed, the systolic time of blood pressure and the inflation/deflation phases of ventilation in anaesthetized pigs are comparable with the extreme values of the considered temporal interval [50 ms, 1 s], respectively ([25], see section 2.2). We found that in all animals and for the whole range of time window sizes, the BA values were above chance level (i.e. >25%). Similar to previous findings [22], we observed statistically significant differences when comparing BA values coming from different electrodes implanted in the same animal (permutation test, $p < 0.05$, $N = 1024$). This effect suggests a role of electrode positioning on decoding performances, hence a spatial functional segregation of vagal fibers, in line with recent findings [40]. We studied the most importance features contributing to BA measure for each active sites. We found that signal power related features, such as MAV, VAR and POW, carry the main contribution to the decrease of trees' impurity. These results are in line with recent findings on different modulation's magnitude of cardiac and respiratory activity

recorded from human VN by using high-selective microneurographic recordings [38]. As an additional evidence of a spatial functional segregation of the VN, we found that not all active sites contribute equally to BA values and we assessed that around the 50% of the active sites lead to a decrease in tree's impurity of the 80%. This highlights the importance of a multichannel intraneuronal electrode approach for a spatially segregated peripheral nerve such as the VN, since the presence of multiple active sites increases the likelihood of an optimal contact with different nerve fibers, which is crucial for detecting informative signals on VN activity.

Interestingly, as shown in figure 3, BA curves in all animals reached a plateau at approximately 500 ms, thus promoting this choice of window size as a good compromise between high performance and a fast computation. In fact, a median BA, over the different test folds, was higher than 85% for all animals. The computational execution time (measured as the time necessary to perform both feature extraction and prediction steps in a single time window) was approximately 6.8 ms (99% percentiles of time windows distribution on a sample animal) resulting in an acceptable time delay as of one order of magnitude lower than the fastest time scale of blood pressure profile like systolic time (~ 50 ms [25]). Regarding BM applications for the cure of cardiovascular diseases, a time window of 500 ms is comparable with the pulse period of blood pressure in anaesthetized pigs [25] thus suitable for closed-loop neuromodulation protocols on such a relevant scale for cardiovascular dynamics.

Our method significantly outperformed (paired *t*-test, $p < 0.001$, $N = 8$) the one proposed previously in [22] and, when comparing our RF classifier to SVM, kNN and MLP, RF performed significantly better than all of them ($p < 0.01$, Kruskal–Wallis test followed by Dunn's post-hoc test, $N = 80$), while kNN resulted to be the model giving the lowest performance ($p < 0.001$, Kruskal–Wallis test followed by Dunn's post-hoc test, $N = 80$). We tested the considered ML models on their robustness to train data-set size decrease of 90%, 80%, 70% of the total training size. We consistently found that RF yielded the best performances and KNN the worst ($p < 0.05$, Kruskal–Wallis test followed by Dunn's post-hoc test, $N = 80$). Our findings are in line with similar findings in the literature [27, 30, 39, 41, 42]. Moreover, even if SVM, kNN and MLP all represent suitable candidates for an on-chip implementation, the memory demand of SVM and kNN scales rapidly with the size of the input [31]. On the other hand, RF allows for an easy parallelization and is power efficient thanks to its implementation based on threshold-based comparisons [6, 31].

Our classification results together with these considerations point to RF as being an ideal candidate

for a future closed-loop BM application in cardio-respiratory diseases.

5. Limitations and future directions

The present analysis was performed by mimicking a pseudo real-time scenario in which a sliding window resembles incoming data to be tested. A necessary step will be the validation of our decoding algorithm in real-time scenarios in future animal experiments.

We employed intraneuronal electrodes which are suitable to perform selective stimulation of different fibers as it was shown in somatic nerves [12, 18–20] and VN stimulation paradigms [25]. Therefore, a promising future direction will be the implementation of closed-loop neuromodulation protocols based on a single intraneuronal interface for decoding and stimulation at the same anatomical point in the VN.

Similarly to [22], we found a dependence of decoding performances on electrode positioning probably due to a spatial segregation of functional fibers [40]. This dependence points out the need of standardized insertion protocols for intraneuronal electrode positioning allowing the target of specific type of functional fibers. Such protocols could be based on recent anatomical and functional reconstruction atlas of the swine VN obtained via microcomputed tomography (CT) and electrical stimulation [40]. Moreover, as suggested in [22], computational modeling of the VN could help to find an optimal anatomical point for decoding and stimulation at the same site.

Our data were collected in an acute setting using anaesthetized animals. In order to develop a valid translational model we will perform future experiments in chronically instrumented, non-anaesthetized animals. Among the possible limitations in chronic settings there could be bio-compatibility and longevity issue of intraneuronal interfaces implanted in VN. Chronic implantation in humans' somatic nerves indicates a reduction in the number of functioning electrode active sites, causing a longitudinal decrease of the signal-to-noise ratio and increase in the stimulation threshold [20]. Promising improvements on robustness, flexibility, and bio-compatibility of intraneuronal interfaces have been achieved in somatic nerves [20] and similar future efforts will be devoted to autonomic nerves.

6. Conclusions

We developed an efficient machine learning model capable of accurately classifying in a short time different physiological states of anaesthetized pigs by using intraneurally recorded neural activity of the VN.

We significantly outperformed our previous approach in terms of accuracy performance [22]. Moreover, our previous approach was not suitable

for real-time applications due to its high computational cost. With the future goal of implementing an on-chip system for BM applications based on closed-loop stimulation, we aimed at keeping the feature extraction procedure simple and a lightweight classification step with an overall low computational execution time.

The present study could represent an important step towards more precise BM neuromodulation protocols via a single intraneuronal interface allowing real-time decoding of physiological conditions combined with selective stimulation of peripheral nerve fibers, thus reducing possible side effects and increasing therapeutic effectiveness.

Data availability statement

The data that support the findings of this study are available upon reasonable request from the authors.

Acknowledgments

This work was partly funded by the Bertarelli Foundation (www.fondation-bertarelli.org) and the EC H2020-FETPROACT-2018-01 NeuHeart (#824071).

Authors contributions

L P analyzed the data, prepared the figures. L P, F V and S Moccia designed the decoding algorithm, interpreted the results and wrote the first draft of the paper. M M O, L C, F V and I S collected the data. I S produced the electrodes. M M O, F A R and S Micera designed the animal experiments. L P, F V, M M O, I S, F A R, S Micera and S Moccia reviewed the paper. F V, S Micera and S Moccia supervised the study. All authors authorized the submission of the manuscript.

ORCID iDs

- Fabio Vallone  <https://orcid.org/0000-0001-8911-9611>
 Matteo M Ottaviani  <https://orcid.org/0000-0002-6354-3278>
 Ivo Strauss  <https://orcid.org/0000-0003-0971-8783>

References

- [1] Birmingham K, Gradinariu V, Anikeeva P, Grill W, Pikov V, McLaughlin B, Pasricha P, Weber D, Ludwig K and Famm K 2014 Bioelectronic medicines: a research roadmap *Nat. Rev. Drug Discovery* **13** 399–400
- [2] Cracchiolo M, Ottaviani M M, Panarese A, Strauss I, Vallone F, Mazzoni A and Micera S 2021 Bioelectronic medicine for the autonomic nervous system: clinical applications and perspectives *J. Neural Eng.* **18** 041002
- [3] Ottaviani M M, Vallone F, Micera S and Recchia F A 2022 Closed-loop vagus nerve stimulation for the treatment of cardiovascular diseases: state of the art and future directions *Front. Cardiovascular Med.* **9** 866957
- [4] Zanos S 2019 Closed-loop neuromodulation in physiological and translational research *Cold Spring Harb. Perspect. Med.* **9** a034314
- [5] Liu Y, Urso A, Martins da Ponte R, Costa T, Valente V, Giagka V, Serdijn W A, Constandinou T G and Denison T 2020 Bidirectional bioelectronic interfaces: system design and circuit implications: system design and circuit implications *IEEE Solid-State Circuits Mag.* **12** 30–46
- [6] Zhu B, Shin U and Shoaran M 2021 Closed-loop neural prostheses with on-chip intelligence: a review and a low-latency machine learning model for brain state detection *IEEE Trans. Biomed. Circuits Syst.* **15** 877–97
- [7] Boon P et al 2015 A prospective, multicenter study of cardiac-based seizure detection to activate vagus nerve stimulation *Seizure* **32** 52–61
- [8] Fisher R S et al 2016 Automatic vagus nerve stimulation triggered by ictal tachycardia: clinical outcomes and device performance—the U.S. E-37 trial *Neuromodulation* **19** 188–95
- [9] Waninger M S, Bourland J D, Geddes L A, Schoenlein W E, Graber G, Weirich W E and Wodigka G R 2000 Electrophysiological control of ventricular rate during atrial fibrillation *Pacing Clin. Electrophysiol.* **23** 1239–44
- [10] Tosato M, Yoshida K, Toft E, Nekrasas V and Struijk J J 2006 Closed-loop control of the heart rate by electrical stimulation of the vagus nerve *Med. Biol. Eng. Comput.* **44** 161–9
- [11] Romero-Ugalde H M, Rolle V L, Bonnet J-L, Henry C, Mabo P, Carrault G and Hernandez A I 2018 Closed-loop vagus nerve stimulation based on state transition models *IEEE Trans. Biomed. Eng.* **65** 1630–8
- [12] Navarro X, Krueger T B, Lago N, Micera S, Stieglitz T and Dario P 2005 A critical review of interfaces with the peripheral nervous system for the control of neuroprostheses and hybrid bionic systems *J. Peripher. Nervous Syst.* **10** 229–58
- [13] Ferrari G M D et al 2017 Long-term vagal stimulation for heart failure: eighteen month results from the neural cardiac therapy for heart failure (NECTAR-HF) trial *Int. J. Cardiol.* **244** 229–34
- [14] Yoo P B, Lubock N B, Hincapie J G, Ruble S B, Hamann J J and Grill W M 2013 High-resolution measurement of electrically-evoked vagus nerve activity in the anesthetized dog *J. Neural Eng.* **10** 026003
- [15] Sevcencu C, Nielsen T N, Kjærgaard B and Struijk J J 2018 A respiratory marker derived from left vagus nerve signals recorded with implantable cuff electrodes *Neuromodulation* **21** 269–75
- [16] Metcalfe B W, Nielsen T N, Donaldson N D N, Hunter A J and Taylor J T 2018 First demonstration of velocity selective recording from the pig vagus using a nerve cuff shows respiration afferents *Biomed. Eng. Lett.* **8** 127–36
- [17] Sevcencu C, Nielsen T N and Struijk J J 2017 A neural blood pressure marker for bioelectronic medicines for treatment of hypertension *Biosens. Bioelectron.* **98** 1–6
- [18] Badia J, Raspopovic S, Carpaneto J, Micera S and Navarro X 2016 Spatial and functional selectivity of peripheral nerve signal recording with the transversal intrafascicular multichannel electrode (TIME) *IEEE Trans. Neural Syst. Rehabil. Eng.* **24** 20–27
- [19] Cutrone A, Valle J D, Santos D, Badia J, Filippeschi C, Micera S, Navarro X and Bossi S 2015 A three-dimensional self-opening intraneuronal peripheral interface (SELINE) *J. Neural Eng.* **12** 016016
- [20] Raspopovic S, Cimolato A, Panarese A, Vallone F, del Valle J, Micera S and Navarro X 2020 Neural signal recording and processing in somatic neuroprosthetic applications. A review *J. Neurosci. Methods* **337** 108653
- [21] Strauss I et al 2020 Q-PINE: a quick to implant peripheral intraneuronal electrode *J. Neural Eng.* **17** 066008
- [22] Vallone F et al 2021 Simultaneous decoding of cardiovascular and respiratory functional changes from pig intraneuronal vagus nerve signals *J. Neural Eng.* **18** 0460a2

- [23] Ottaviani M M, Wright L, Dawood T and Macefield V G 2020 *In vivo* recordings from the human vagus nerve using ultrasound-guided microneurography *J. Physiol.* **598** 3569–76
- [24] Marmorstein J T, McCallum G A and Durand D M 2022 Decoding vagus-nerve activity with carbon nanotube sensors in freely moving rodents *Biosensors* **12** 114
- [25] Sevcencu C, Nielsen T N and Struijk J J 2018 An intraneuronal electrode for bioelectronic medicines for treatment of hypertension *Neuromodulation* **21** 777–86
- [26] Wang X, Gong G, Li N and Qiu S 2019 Detection analysis of epileptic EEG using a novel random forest model combined with grid search optimization *Front. Hum. Neurosci.* **13** 52
- [27] Turner A, Shieff D, Dwivedi A and Liarokapis M 2021 Comparing machine learning methods and feature extraction techniques for the EMG based decoding of human intention 2021 43rd Annual Int. Conf. IEEE Engineering in Medicine Biology Society (EMBC) pp 4738–43
- [28] Luu D K, Nguyen A T, Jiang M, Xu J, Drealan M W, Cheng J, Keefer E W, Zhao Q and Yang Z 2021 Deep learning-based approaches for decoding motor intent from peripheral nerve signals *Front. Neurosci.* **15** 667907
- [29] Koh R G L, Nachman A I and Zariffa J 2019 Classification of naturally evoked compound action potentials in peripheral nerve spatiotemporal recordings *Sci. Rep.* **9** 11145
- [30] Douglas P, Harris S, Yuille A and Cohen M S 2011 Performance comparison of machine learning algorithms and number of independent components used in fMRI decoding of belief vs. disbelief *NeuroImage* **56** 544–53
- [31] Shoaran M, Hagh B A, Taghavi M, Farivar M and Emami-Neyestanak A 2018 Energy-efficient classification for resource-constrained biomedical applications *IEEE J. Emerg. Sel. Top. Circuits Syst.* **8** 693–707
- [32] Zhu B, Farivar M and Shoaran M 2020 ResOT: resource-efficient oblique trees for neural signal classification *IEEE Trans. Biomed. Circuits Syst.* **14** 692–704
- [33] Hill D N, Mehta S B and Kleinfeld D 2011 Quality metrics to accompany spike sorting of extracellular signals *J. Neurosci.* **31** 8699–705
- [34] Zhuang K Z et al 2019 Shared human–robot proportional control of a dexterous myoelectric prosthesis *Nat. Mach. Intell.* **1** 400–11
- [35] Raspopovic S, Carpaneto J, Udina E, Navarro X and Micera S 2010 On the identification of sensory information from mixed nerves by using single-channel cuff electrodes *J. Neuroeng. Rehabil.* **7** 17
- [36] Hong K-S, Aziz N and Ghafoor U 2018 Motor-commands decoding using peripheral nerve signals: a review *J. Neural Eng.* **15** 031004
- [37] Zanos T P, Silverman H A, Levy T, Tsavas T, Battinelli E, Lorraine P W, Ashe J M, Chavan S S, Tracey K J and Bouton C E 2018 Identification of cytokine-specific sensory neural signals by decoding murine vagus nerve activity *Proc. Natl Acad. Sci.* **115** E4843–52
- [38] Patros M, Ottaviani M M, Wright L, Dawood T and Macefield V G 2022 Quantification of cardiac and respiratory modulation of axonal activity in the human vagus nerve *J. Physiol.* **600** 3113–26
- [39] Anam K, Nuh M and Al-Jumaily A 2019 Comparison of EEG pattern recognition of motor imagery for finger movement classification 6th Int. Conf. on Electrical Engineering, Computer Science and Informatics (EECSI) pp 24–27
- [40] Jayaprakash N et al 2022 Organ- and function-specific anatomical organization and bioelectronic modulation of the vagus nerve *bioRxiv Preprint* (<https://doi.org/10.1101/2022.03.07.483266>) (posted online 30 March 2022)
- [41] Ma S, Jin D, Zhang M, Zhang B, Wang Y, Li G and Yang M 2019 Silent speech recognition based on surface electromyography 2019 Chinese Automation Congress (CAC) pp 4497–501
- [42] Samanta K, Chatterjee S and Bose R 2020 Cross-subject motor imagery tasks EEG signal classification employing multiplex weighted visibility graph and deep feature extraction *IEEE Sens. Lett.* **4** 1–4